Journal of Geophysical Research: Planets

RESEARCH ARTICLE

Key Points:
- We measure thermal conductivity of H_2O-CH_3OH mixtures to 12 GPa
- Thermal conductivity of ice VII-CH_3OH are substantially reduced
- Ten weight percent CH_3OH in ice mantle of super-Earths reduces twice the power transported by convection

Correspondence to:
W.-P. Hsieh,
wphsieh@earth.sinica.edu.tw

Thermal conductivity of H₂O-CH₃OH mixtures at high pressures: Implications for the dynamics of icy super-Earths outer shells

Wen-Pin Hsieh[1] and Frédéric Deschamps[1]

[1]Institute of Earth Sciences, Academia Sinica, Nankang, Taipei, Taiwan

Abstract Thermal conductivity of H_2O-volatile mixtures at extreme pressure-temperature conditions is a key factor to determine the heat flux and profile of the interior temperature in icy bodies. We use time domain thermoreflectance and stimulated Brillouin scattering combined with diamond anvil cells to study the thermal conductivity and sound velocity of water (H_2O)-methanol (CH_3OH) mixtures to pressures as high as 12 GPa. Compared to pure H_2O, the presence of 5–20 wt % CH_3OH significantly reduces the thermal conductivity and sound velocity when the mixture becomes ice VI-CH_3OH and ice VII-CH_3OH phases at high pressures, indicating that the heat transfer is hindered within the icy body. We then apply these results to model the heat transfer through the icy mantles of super-Earths, assuming that these mantles are animated by thermal convection. Our calculations indicate that the decrease of thermal conductivity due to the presence of 10 wt % CH_3OH induces a twofold decrease of the power transported by convection.

1. Introduction

The detection of super-Earths, defined as exoplanets with masses in the range of 1 to 10 Earth mass, opened a whole new field of study, in particular to model their interior. Assuming that they are differentiated; i.e., denser materials have migrated toward their center, super-Earths may consist of a core of metals, surrounded by a rocky mantle and, in some cases, an icy mantle. The radial structure of super-Earths may thus be modeled by solving a set of differential equations for density, gravity, mass, pressure, and temperature, together with a *P-V-T* equation of state relating density to pressure and temperature [e.g., *Sotin et al.*, 2007; *Valencia et al.*, 2007a, 2007b]. For a given composition in metals, rocks, and ices, these models provide mass-radius relationships.

If formed beyond the snowline of their stellar system, super-Earths may have retained enough water to form an outer shell of water [*Kuchner*, 2003; *Léger et al.*, 2004]. Whether this shell is liquid (ocean planet), or partially or entirely solid (icy super-Earth) depends on several parameters, including the surface temperature, the thermal history of the planet (which depends in turn on the ability of the different layers to transport heat toward the surface), and the presence of volatiles compounds, particularly antifreeze compounds such as ammonia (NH_3) and methanol (CH_3OH), which are likely to stop or delay the crystallization of the water layer as the planet is cooling down. In the conditions of the solar nebula in the outer solar system, volatiles may have been trapped in planetesimals from which icy moons have been formed. Condensation models indicate that methanol and ammonia may be present in these planetesimals with concentration of 4.0 wt % and 1.0 wt %, respectively [*Mousis et al.*, 2009; *Deschamps et al.*, 2010]. The presence of volatile compounds within icy moons is further supported by spectroscopic observations of comets, which are supposed to be planetesimals remnants, with abundances relative to water up to 10 wt % for methanol and 2 wt % for ammonia [*Mumma and Charnley*, 2011]. Interestingly, both methanol and ammonia have also been detected in the gas plumes of Enceladus [*Waite et al.*, 2009; *Hodyss et al.*, 2009].

As in the case of icy moons of giant planets, for which detailed models of possible radial structure and thermal evolution have been calculated (for a review, see *Hussmann et al.* [2007]), this may result in a radial structure consisting of a thin outer ice I shell, a residual ocean, and a shell of high pressure ices surrounding the rocky mantle. A major difference, however, is that the size and gravity of super-Earths allows very high pressure phases (VI, VII, X, and XI) of ices to form at the bottom of the outer shell.

Accurate modeling of icy super-Earth interiors requires knowledge of physical and thermo-chemical properties of high pressure ices. *Fei et al.* [1993] measured the density, thermal expansion coefficient, and phase diagram
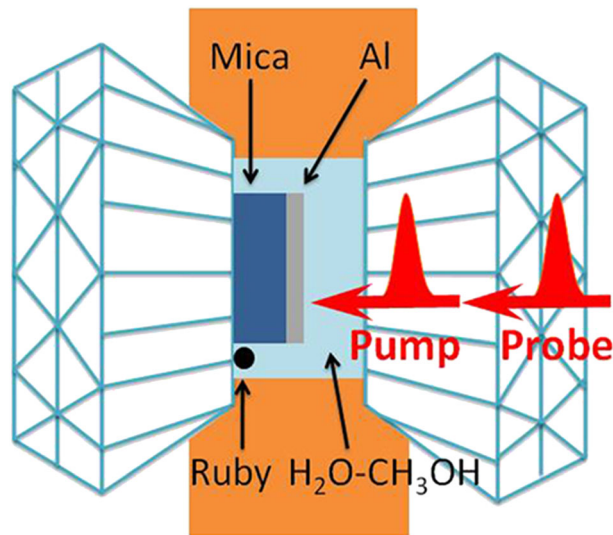
Figure 1. Schematic illustration of the optical measurements (TDTR and picosecond interferometry) coupled with a diamond anvil cell. The H_2O-CH_3OH mixture serves as the pressure transmitting medium and sample of interest, and the mica is a substrate coated with Al film that absorbs thermal energy from optical pump and probe beams. The pressure is measured by ruby fluorescence.

of ice VII, allowing the construction of a P-V-T equation of state. Because it influences heat transfer through ice layers, thermal conductivity is another key parameter. For ice VII, the experiments of *Chen et al.* [2011] showed that the thermal conductivity increases by nearly 1 order of magnitude between 2 and 22 GPa. Importantly, these properties may strongly depend on the presence of volatiles. Ammonia and methanol both decrease the crystallization temperature of water, which may substantially affect the radial structure of icy moons, dwarf planets, and icy super-Earths. In the case of icy moons and dwarf planets, models of thermal evolution showed that antifreeze compounds, even in small quantities (typically a few weight percent), may result in the formation of residual subsurface ocean [e.g., *Grasset et al.*, 2000; *Deschamps et al.*, 2010]. So far, however, very little experimental data for the thermal conductivity of water-volatile mixtures at extreme pressures are available. Here we report measurements of thermal conductivity of the H_2O-CH_3OH system at room temperature and up to 12 GPa. Our results show that compared to pure H_2O, the presence of small amounts (5–20 wt %) of CH_3OH substantially decreases the thermal conductivity of H_2O ice VII-CH_3OH mixtures by a factor of 2 to 5. We then apply these results to model the heat transfer through ice mantles of icy super-Earths and find that the decrease in thermal conductivity due to the presence of 10 wt % CH_3OH induces a twofold decrease in convective power transport, demonstrating the marked influence of volatiles in the thermal evolution of icy bodies.

2. Experimental Details

To measure the thermal conductivity of water (H_2O)-methanol (CH_3OH) mixtures at high pressures, a 20 μm thick sheet of muscovite mica, $KAl_2(Si_3Al)O_{10}(OH)_2$ (grade V-1 from SPI Supplies) was coated with 80 nm thick Al film and loaded into a symmetric diamond anvil cell (DAC) with culet size of 500 μm. The muscovite mica served as a reference substrate and thermal insulator and was pressurized by loading distilled H_2O mixed with specific weight percent of CH_3OH (see Figure 1 for the schematic illustration of the sample within a DAC). The pressure was determined by fluorescence spectrum of a ruby ball [*Mao et al.*, 1978] that was also loaded into the DAC. With this experimental setup, the typical uncertainties of the pressure measurements were ~0.1 GPa. After the pressure within the DAC equilibrated, the high-pressure thermal conductivity of H_2O-CH_3OH mixtures was measured at room temperature using time domain thermoreflectance (TDTR). In the TDTR measurement, the laser beam from a Ti:sapphire oscillator was split into pump and probe beams. The pump beam, electrooptically modulated at 8.7 MHz, heats the Al film on the muscovite substrate, and the time-delayed probe beam then monitors the resulting temperature variations on the Al film through changes in the optical reflectivity. The in-phase V_{in} and out-of-phase V_{out} components of the small variations of the reflected probe beam intensity that are synchronous with the 8.7 MHz modulation frequency of the pump beam were measured using a Si fast photodiode as well as RF lock-in amplifier. The details of the TDTR are described in *Cahill et al.* [2003] and *Hsieh et al.* [2009].

We determined the thermal conductivity of H_2O-CH_3OH mixture by comparing the ratio $-V_{in}/V_{out}$ as a function of delay time between pump and probe beams to calculations based on a thermal model that takes into account heat flow into the H_2O-CH_3OH mixture and into the muscovite mica substrate [*Cahill*, 2004; *Ge et al.*, 2006].

Figure 2. (a) Example data for the ratio $-V_{in}/V_{out}$ as a function of delay time between pump and probe beams at high pressures and fits (solid lines) to the thermal model that considers bidirectional heat flow. (b) Example data for the periodic oscillations in V_{in} signals at high pressures. The Brillouin frequency of the H_2O-CH_3OH mixture is determined by the inverse of the period. Pressure is labeled next to each datum.

The thermal model for such bidirectional heat flow contains several parameters, such as laser spot size, modulation frequency of the pump beam, thickness of Al film, thermal conductivity, and heat capacity of each material layer, but the thermal conductivity of H_2O-CH_3OH mixture is the only significant unknown and free parameter to be determined. We in situ measured the thickness of Al film at ambient pressure by picosecond acoustics [*O'Hara et al.*, 2001] and estimated the changes in Al film thickness under pressure following a method described in *Chen et al.* [2011]. We evaluated the heat capacity of Al as a function of pressure from data for the pressure dependence of atomic density and elastic constants as well as calculations of Debye temperature [*Hsieh et al.*, 2009]. The thermal conductivity and heat capacity of muscovite mica at room temperature and high pressures were taken from *Hsieh et al.* [2009].

The heat capacity of H_2O mixed with low-content CH_3OH at high pressures is not known. Due to the dominant molar fraction of H_2O in the mixture, we assume that the pressure dependence of specific heat capacity of H_2O-CH_3OH mixtures is close to that of the pure H_2O, which was calculated using density functional theory [*Chen et al.*, 2011]. Uncertainties in all the parameters used in the thermal model propagate to ~5% error in the measured thermal conductivity of the H_2O-CH_3OH mixtures in the low-pressure regime and to less than 15 % error at the highest pressure we measured. Example data and fits to the thermal model at high pressures are shown in Figure 2a.

We then measured the Brillouin frequency of H_2O-CH_3OH mixture by time domain stimulated Brillouin scattering [*Hsieh et al.*, 2009; *O'Hara et al.*, 2001; *Thomsen et al.*, 1986], which is an inelastic light scattering from acoustic modes that probes the sound velocity and elastic constants of a material. For longitudinal modes in a backscattering geometry, the Brillouin frequency is

$$f_B = 2Nv_l/\lambda, \tag{1}$$

where N is the index of refraction, v_l is the longitudinal sound velocity, and $\lambda = 785$ nm is the laser wavelength. In our experiments, the pump pulses heat the Al film and the thermal expansion of Al generates a strain wave. Constructive interference of the probe pulses reflected from the strain wave and from the Al surface results in periodic oscillations in the in-phase signal V_{in} with frequency f_B. Example data for the measurements of Brillouin frequency are shown in Figure 2b. The typical uncertainty of the measured Brillouin frequency is ~1%.

3. Results

Figure 3a shows the pressure dependence of Brillouin frequency of H_2O-CH_3OH mixtures with various CH_3OH content. In the same experimental runs, we also used Raman spectroscopy to characterize the high-pressure behavior of the mixtures and observed consistent phase transition pressures and Raman frequency shifts as reported in *Hsieh and Chien* [2015]. We did not observe pressure-induced crystallization of CH_3OH, suggesting that the CH_3OH was superpressed under our experimental conditions. To derive the longitudinal sound velocity v_l of H_2O-CH_3OH mixtures, we assumed that the index N of H_2O mixed with low-content CH_3OH is the same as that of pure H_2O, which was taken from the results in *Pan et al.* [2014] and *Shimizu et al.* [1996]. Note
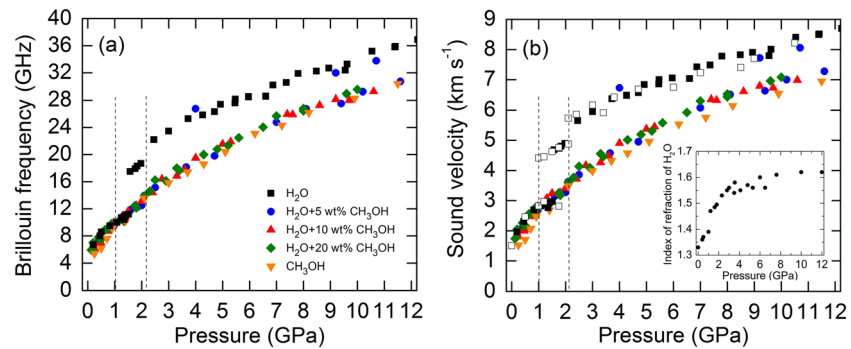
Figure 3. Pressure dependence of the (a) Brillouin frequency and (b) longitudinal sound velocity of H_2O-CH_3OH mixtures. The Brillouin frequency and sound velocity are weakly dependent on the CH_3OH content and lower than those for pure H_2O, in particular when the water crystallizes to ice VI and ice VII. Data for pure CH_3OH [*Hsieh*, 2015] (orange lower triangles) are plotted for comparison. The dashed lines mark the phase transition pressures of pure water to ice VI and ice VII phases that are taken from *Chen et al.* [2011]. In Figure 3b we also plot the pressure dependence of sound velocity of pure H_2O by *Polian and Grimsditch* [1983] (open squares) and index of refraction of H_2O taken from *Pan et al.* [2014] and *Shimizu et al.* [1996] in the inset, respectively.

that the index *N* of pure H_2O is nearly the same as pure CH_3OH at ambient pressure and is similar to a CH_3OH-dominant compound (4:1 methanol-ethanol mixture) over the pressure range we studied [*Eggert et al.*, 1992]. As shown in Figure 3b, the v_l of pure H_2O (black squares) increases dramatically upon the pressure induced crystallization to ice VI and ice VII phases, in good agreement with the results derived from *Polian and Grimsditch* [1983]. In our experiments, liquid water persisted beyond 1 GPa due to steady state heating on the sample by the incident pump and probe beams. For liquid water, we estimate $\Delta T \approx 50$ K. The steady state heating reduces to $\Delta T \approx 30$ K for ice VI and $\Delta T < 20$ K for ice VII, respectively.

Recent experiments [*Hsieh and Chien*, 2015] reported that the high-pressure crystallization behavior and intermolecular bonding of H_2O-CH_3OH mixtures are different from those of the pure H_2O. The phase transition pressures for liquid water-ice VI and ice VI-VII phases vary with the CH_3OH content in the mixture (see Figure 7 in *Hsieh and Chien* [2015]). Here we find that the pressure evolution of longitudinal sound velocity is also significantly changed when H_2O is mixed with low content CH_3OH (Figure 3b). When the H_2O is in liquid phase, the v_l of all H_2O-CH_3OH mixtures are slightly lower than the v_l of pure H_2O by about 5–10%. Upon further compression, the v_l of all H_2O-CH_3OH mixtures increase with pressure, but only show a nominal increase as the water crystallizes to ice VI and ice VII, resulting in a marked reduction in the v_l by about 20–30 % compared to the v_l of pure H_2O. Note that some of the measured v_l of H_2O ice VII mixed with 5 wt % CH_3OH are close to the pure H_2O ice VII; we attribute these results that are similar to pure ice VII to the possible pressure-induced molecular segregation of CH_3OH from the ice VII [*Hsieh and Chien*, 2015] that occurs in all the mixtures with 5–20 wt % CH_3OH. For the 5 wt % CH_3OH mixture, after the inhomogeneous molecular distribution occurs, a local sample area ($\approx 8 \mu m$) probed by optical pulses may be largely composed of H_2O ice VII, and under such circumstances the effect of such small amount of CH_3OH on the Brillouin frequency and sound velocity is minimal. However, for mixtures with 10 and 20 wt % CH_3OH, the relatively abundant CH_3OH molecules (compared to 5 wt %) could form a locally connected phase that substantially lowers the effective Brillouin frequency and sound velocity of the mixtures.

The pressure dependence of thermal conductivity and thermal effusivity of H_2O-CH_3OH mixtures are presented in Figures 4a and 4b. The thermal conductivity of pure H_2O (black squares) increases with pressure and undergoes two sharp increase upon crystallization to ice VI and ice VII phases, consistent with literature data (open squares) [*Chen et al.*, 2011]. Similar to the sound velocity measurements, the thermal conductivity of H_2O-CH_3OH mixtures is slightly lower than that of the pure H_2O by about 10% as the H_2O is in liquid phase. The thermal conductivity, however, increases with pressure without dramatic increase across phase transitions to ice VI and VII and is lower than the thermal conductivity of pure H_2O by about 35% in the ice VI-CH_3OH phase, and by a factor of 2 to 5 as the mixture becomes the ice VII-CH_3OH phase. Such reduction in the thermal conductivity is enhanced with CH_3OH content. Note that the thermal conductivity of H_2O-5 wt % CH_3OH shows a relatively larger variation, likely due to the pressure-induced inhomogeneous distribution of H_2O and CH_3OH molecules within the sample
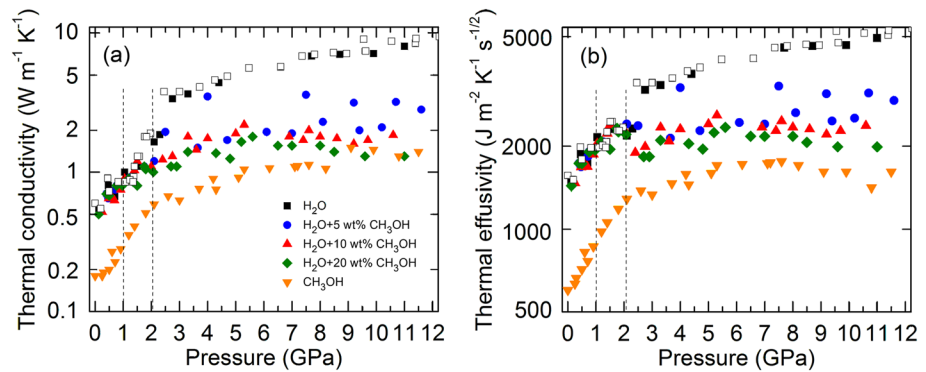
Figure 4. Pressure dependence of the (a) thermal conductivity and (b) thermal effusivity of H_2O-CH_3OH mixtures. Thermal conductivities and effusivities of ice VI-CH_3OH and ice VII-CH_3OH mixtures are substantially reduced compared to those of pure ice VI and ice VII. Data for pure H_2O [*Chen et al.*, 2011] (open squares) and for pure CH_3OH [*Hsieh*, 2015] (orange lower triangles) are plotted for comparison. The dashed lines mark the phase transition pressures of pure water to ice VI and ice VII phases that are taken from *Chen et al.* [2011].

chamber in which a local sampling area may be largely composed of H_2O ice VII and the influence of small amount of CH_3OH on the thermal conductivity is minimal. The presence of low-content (5–20 wt %) CH_3OH in H_2O and the possible pressure-induced inhomogeneous molecular distribution could also serve as additional scattering mechanisms for the heat transport within the mixture.

4. Implications for Icy Super-Earths

Heat transfer through ice shells, for instance the outer shells of icy moons and dwarf planets, or hypothetical icy mantles of super-Earths, is strongly influenced by the physical properties of high-pressure ices, including their thermal conductivity. In this section, we discuss the influence of ice VII thermal conductivity on the heat transfer through the icy mantle of super-Earths, assuming that this mantle is animated by thermal convection. Note that the presence of a connected phase of CH_3OH within H_2O ice VII (see section 3) may complicate the dynamics of the ice mantle. If it is globally connected, CH_3OH may gravitationally segregate at the bottom of the shell, and the ice layer alone may be animated by convection. On another hand, local connections would result in a two-phase system, inducing important changes in the flow structure and heat transfer compared to the stagnant lid convection, which we assumed in the calculations below.

We consider super-Earths with radial structure consisting of a metallic core surrounded successively by a rocky (silicate) mantle, a layer of high-pressure ices (ice VI and VII), and a global ocean. We first used the mass-radius relationships of *Valencia et al.* [2007b] to calculate the radius of the planet as a function of its total mass (M_P) and of its mass fraction of water, defined as the ratio of the mass of water (M_{H2O}) to the total mass of the planet, $x_{H2O} = M_{H2O}/M_P$. We set the surface temperature, T_{surf}, to 300 K and assume that the adiabatic increase of temperature through the external ocean is negligible (i.e., the temperature at the top of the ice mantle is also equal to 300 K). We determined the depth of the bottom of the ocean (top of the ice mantle) from the melting curves of ices Ih-VI [*Chizhov*, 1993] and ice VII [*Pistorius et al.*, 1963]. The presence of CH_3OH substantially modifies the melting curve of ice VII. Recent experiments [*Hsieh and Chien*, 2015] indicate that at $T = 300$ K, the liquid/solid transition pressure, which is equal to 1.0 GPa for pure water, increases by 0.5 GPa and 1.0 GPa if methanol is added by 5 wt % and 10 wt %, respectively. Note that the amount of methanol is here relative to the amount of water. The depth of the bottom of the high-pressure ice mantle is controlled by the mass fraction of water (x_{H2O}). To calculate this depth, we accounted for compressibility, using the equation of state of ice VII by *Fei et al.* [1993]. Figure 5a plots the thickness of the high-pressure ices mantle as a function of x_{H2O}, and for two values of M_P, corresponding to 1 and 2 Earth masses. We consider two compositions for the outer shells, pure water (plain curves), and H_2O-10 wt % CH_3OH (dashed curves). In the latter case, the depth of the top of the ice layer is calculated by increasing the pressure of the liquid to solid transition by 1.0 GPa compared to the pure water case [*Hsieh and Chien*, 2015], leading to slightly thinner ice mantles, typically by 50 to 100 km.
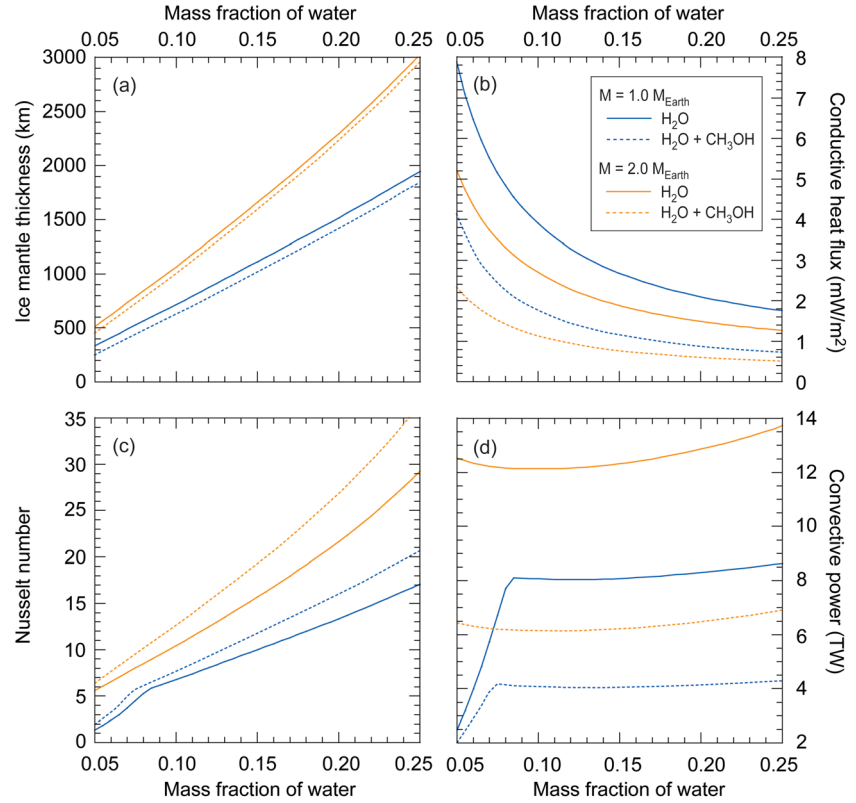
Figure 5. Heat transfer through super-Earths with mass equal to 1.0 M_{Earth} (blue curves) and 2.0 M_{Earth} (orange curves). Results are plotted as a function of the mass fraction of water. Plain and dashed curves denote pure water and a H_2O-10 wt % CH_3OH mixture, respectively. (a) Thickness of the ice mantle. (b) Conductive heat flux. (c) Nusselt number. (d) Convective power. See text for details of the calculations.

The convective heat flux at the bottom of the ice mantle, Φ_{conv}, and the total power transported by convection, P, are given as a function of the conductive heat flux by

$$\Phi_{conv} = Nu \ \Phi_{cond}/f \qquad (2)$$

and

$$P = 4\pi r_{in}^2 \ \Phi_{conv}, \qquad (3)$$

where r_{in} is the inner radius of the ice mantle, Φ_{cond} is the conductive heat flux at the base of this mantle, Nu is the Nusselt number, measuring the efficiency of the convective heat transfer relatively to the conductive heat transfer, and f a geometrical factor introduced by spherical geometry and defined as the ratio of the inner to outer radii of the shell, $f = r_{in}/r_{out}$. In spherical geometry, Φ_{cond} is given by

$$\phi_{cond} = \frac{k\Delta T_S}{Df} \qquad (4)$$

where k is the thermal conductivity of the ice, D is the thickness of the ice mantle, and ΔT_S is the temperature jump across it. The Nusselt number depends on the details of the convective flow, which in turn depend on the properties of the fluid. Here we assumed that convection in the ice mantle operates in the stagnant lid regime, which is characteristic of fluid experiencing large viscosity variations with temperature, as is the case for high-pressure ices [e.g., *Durham and Stern*, 2001]. This regime of convection has been numerically studied in various geometries [e.g., *Solomatov*, 1995; *Reese et al.*, 1999; *Deschamps and Lin*, 2014], and recent numerical experiments in spherical shells [*Yao et al.*, 2014] indicate that the Nusselt number is well described by

$$Nu = \frac{1.46Ra_m^{0.27}}{\gamma^{1.21}f^{0.78}} \qquad (5)$$

where Ra_m is the Rayleigh number of the convective interior and γ is a viscous temperature scale controlling the temperature jump in the top thermal boundary layer, and related to the amplitude of viscosity variations [*Davaille and Jaupart*, 1993]. The value of γ depends on the rheology of ice, and in particular its activation energy. The Rayleigh number is defined by

$$Ra_m = \frac{\alpha \rho g \Delta T_S D^3}{\kappa \eta_m},$$ (6)

where α is the thermal expansion coefficient, ρ is the density, g is the gravity acceleration, κ is the thermal diffusivity, and η_m is the viscosity taken at the temperature of the well-mixed interior, T_m. This temperature is defined as

$$T_m = T_{\text{surf}} + b \Delta T_S,$$ (7)

where b is a parameter that measures the temperature jump in the top half of the system (including in the case of stagnant lid convection, the top thermal boundary layer and the stagnant lid) and that depends on the physical properties of the system. For an isoviscous fluid in Cartesian geometry the temperature jumps in the top and bottom thermal boundary layers are equal, and therefore, $b = 0.5$. For spherical shells animated with stagnant lid convection, *Yao et al.* [2014] showed that the value of b depends on both the ratio f and the viscous temperature scale γ. For icy shells and mantles, where $0.7 \leq f \leq 0.9$ and γ is around 20, b is in the range between 0.8 and 0.9. Here we assumed $b = 0.85$.

For calculations, we considered two values of the thermal conductivity, $k = 5.0 \, \text{W m}^{-1} \, \text{K}^{-1}$ for the pure water case, and $k = 2.0 \, \text{W m}^{-1} \, \text{K}^{-1}$ for a H_2O-10 wt % CH_3OH mixture. These values correspond to average values in the pressure range of 2–12 GPa (Figure 4). The gravity acceleration is calculated as a function of the planet's mass and radius, the latter being derived from the mass-radius relationships of *Valencia et al.* [2007b]. The geometric factor f is simply derived from the depths of the top and bottom of the ice mantle. The superadiabatic temperature jump through the ice mantle, ΔT_S, is treated as a free parameter. Fixing the surface temperature, as we do here, the value of ΔT_S is controlled by the temperature at the bottom of the ice shell and therefore by the thermal history (cooling) of the planet. This cooling depends in turn on the amount of heat available at the bottom of the ice mantle (resulting, in particular, from radiogenic heating in the rocky mantle below the ice shell, and from the cooling of the core) and on the ability of this mantle to transport the heat toward the surface. Modeling the thermal history of icy super-Earths is beyond the scope of this study and may not result in better constrained values of ΔT_S since it depends on many unknown or poorly constrained parameters. In our case, however, the fact that we impose the presence of a thick ice mantle at the top of the super-Earth implicitly assumes a relatively efficient cooling of the planet through time (since it allows the crystallization of an icy mantle) and implies that the superadiabatic temperature jump in the ice mantle should not be too high, so that ice does not melt at the bottom of the ice mantle. Note that ΔT_S may substantially influence the convection and heat transfer through the ice mantle because it appears in the expression of the Rayleigh number (with higher ΔT_S leading to higher Rayleigh number, thus more vigorous convection) and more importantly, because it controls the temperature of the well-mixed interior T_m (equation (7)) and therefore the bulk viscosity. Here we fixed ΔT_S to 300 K, unless this value implies that the temperature at the bottom of the ice mantle, $T_{\text{bot}} = T_{\text{surf}} + \Delta T_S$, is larger than the melting temperature of ice VII, T_{melt}. In the latter case, which occurs for thin ice mantles (i.e., small values of x_{H2O}), we adjusted ΔT_S according to the melting curve of ice VII following $\Delta T_S = T_{\text{melt}} - T_{\text{surf}}$. For $\Delta T_S = 300$ K and $b = 0.85$, equation (7) implies that the temperature of the well-mixed convective interior, T_m, is equal to 555 K. To calculate the Rayleigh number, we then fixed the density, ρ, and the thermal expansion coefficient, α, to $\rho = 1520 \, \text{kg m}^{-3}$ and $\alpha = 2.8 \times 10^{-4} \, \text{K}^{-1}$, which correspond to the values of these parameters at 2.2 GPa and 550 K according to *Fei et al.* [1993] measurements and equation of state for ice VII. Thermal diffusivity κ, the ratio of thermal conductivity to volumetric heat capacity, was deduced from our experimental data for thermal conductivity, leading to $\kappa = 2.0 \times 10^{-6} \, \text{m}^2 \, \text{s}^{-1}$ for pure water and $\kappa = 0.8 \times 10^{-6} \, \text{m}^2 \, \text{s}^{-1}$ for a H_2O-10 wt % CH_3OH mixture. The most sensitive parameter in the definition of the Rayleigh number is, together with the thickness of the ice mantle, the viscosity of the well-mixed interior, η_m. Here we fixed its value according to the experiments on the rheology of ice VI [*Durham et al.*, 1996], for which the activation energy of the high-temperature regime at 2.2 GPa is equal to 134.2 kJ mol^{-1}. At low stress ($\sigma = 0.01$ MPa), which is typical of convection in ice layers of icy moons [*Durham and Stern*, 2001], and temperature $T_m = 555$ K, the high-temperature regime of *Durham et al.* [1996] predicts an effective viscosity (defined as

half the ratio between the stress and the strain rate) of $\eta_m = 4.2 \times 10^{18}$ Pa s. Note that in cases where ΔT_S (and thus T_m) is decreased to avoid melting at the bottom of the ice mantle, η_m increases (by about one order of magnitude if ΔT_S is decreased to 250 K), implying smaller Rayleigh number. More importantly, because viscosity strongly depends on stress and temperature, which are not well constrained, its value is highly uncertain and may vary by 1 order of magnitude or more. Furthermore, at low stress the rheology of ice VII may be Newtonian, instead of non-Newtonian as observed by *Durham et al.* [1996], which may further modify ice VII viscosity and its sensitivity to temperature. A more detailed study, beyond the scope of this paper, would be required to explore these effects. It should be pointed out, however, that the value we estimate here provides reasonable values for the Rayleigh number and the quantities derived from it (Nusselt number, power transported by convection), and is well suited for our purpose. The viscous temperature scale γ in the Nusselt number equation (equation (5)) depends on the activation energy of ice, and on ΔT_S and T_m [*Deschamps et al.*, 2010; *Yao et al.*, 2014]. Using the values defined above, we get $\gamma = 17.51$, corresponding to a top to bottom thermal viscosity ratio of 7.0×10^6.

Figures 5b and 5c show the conductive heat flux (equation (4)), and Nusselt number (equation (5)) as a function of the mass fraction of water in the planet, x_{H2O}. The conductive heat flux decreases with x_{H2O}, due to the fact that all other parameters being equal, the thickness of the ice mantle increases with x_{H2O} (Figure 5a). Furthermore, for a given mass fraction of water, the conductive heat flux decreases as the mass of the planet, M_P, increases. Again, this is related to the fact that for a given value of x_{H2O}, the amount of ice, and therefore the thickness of the ice mantle, increases with M_P (Figure 5a). By contrast, the vigor of convection, measured by the Rayleigh number (equation (6)), increases with the thickness of ice layer. In addition, the ratio between the inner and outer radii of the ice mantle, f, decreases as the thickness of this mantle increases. As a consequence, according to equation (5), the Nusselt number increases with both M_P and x_{H2O}. The change of behavior in the Nusselt number around $x_{H2O} = 0.08$ for $M_P = 1.0$ (plain blue curve) is related to a change in the superadiabatic temperature jump. For $x_{H2O} < 0.08$, a ΔT_S of 300 K, as assumed in the rest of the calculations, induces melting at the bottom of the ice mantle, and we therefore changed its value to $T_{melt} - T_{surf}$.

The presence of CH_3OH influences heat transfer in different ways. First, adding 10 wt % CH_3OH in water shifts the liquid to solid transition pressure by 1.0 GPa, resulting in thinner high-pressure ice mantles (Figure 5a). Second, it decreases the thermal conductivity (and the thermal diffusivity) by a factor of approximately 2 to 5 (Figure 4). These two effects are opposing each other and have opposite influence on the conductive heat flux and on the convective heat transfer. The conductive heat flux (equation (4)) slightly increases as the icy mantle thins, but this increment is small and is overrun by the drop in thermal conductivity. By contrast, the Rayleigh number (equation (6)) slightly decreases as the ice mantle thins, but again, this change is small and is fully compensated by decrease in thermal diffusivity. Overall, the conductive heat flux decreases with the presence of CH_3OH (Figure 5b), whereas the Rayleigh number, and therefore the Nusselt number (equation (5); Figure 5c) increase. All other parameters being equal, the presence of 10 wt % CH_3OH decreases the conductive heat flux by about a factor of 2 and increases the Nusselt number by about 20%.

The convective heat flux (equation (2)) and transported power (equation (3)) result from the competition between the Nusselt number and the conductive heat through the ice layer, which are respectively increasing and decreasing with the ice mantle thickness (or, equivalently, with x_{H2O}; see Figure 5a). Overall, the transported power (Figure 5d) does not vary substantially with x_{H2O}, except for $M_P = 1.0$ and $x_{H2O} < 0.08$. By contrast, the mass of the planet has a stronger influence, with more massive planets allowing a better convective heat transfer through the ice mantle. For pure water, the power increases from about 8 TW for $M_P = 1.0\ M_{Earth}$ to 13 TW for $M_P = 2.0\ M_{Earth}$. Thermal conductivity also has a strong influence on the heat transfer. A decrease in this parameter by a factor of 2.5, due in our case to the presence of 10 wt % CH_3OH, strongly decreases the conductive heat flux (Figure 5b) and results in a drop of the convective power by about a factor of 2.

Figure 6 shows the pressure at the bottom of the ice shell as a function of the fraction of water (x_{H2O}), and for different values of the super-Earth's mass. One may point out that for most cases this pressure exceed our experimental pressure range (2–12 GPa), denoted by the grey shaded area in Figure 6. When applying our experimental data to icy super-Earths, we therefore assume that these results can be extrapolated to higher pressures, which may be a source of uncertainties. It should be pointed out, however, that for pressures larger than 5 GPa and up to 12 GPa, the thermal conductivity of H_2O-CH_3OH mixtures increases very weakly with pressure. In contrast, the increase of thermal conductivity of pure H_2O with pressure is more significant (Figure 4a).
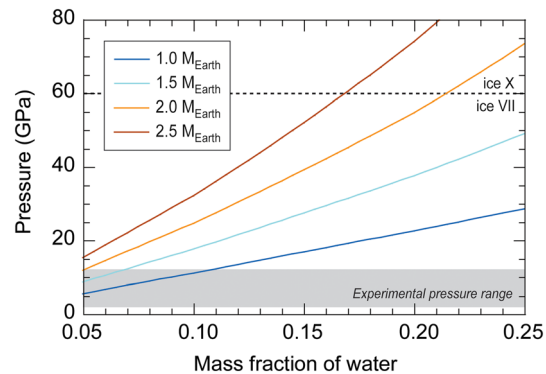
Figure 6. Pressure at the bottom of the ice shell as a function of the mass fraction of water and for several values of the super-Earth's mass (color code). For comparison, the pressure range of our experiments (2–12 GPa) is indicated with the grey shaded area. The thick dashed line around 60 GPa denotes the boundary between the ice VII and ice X phases [*Goncharov et al.*, 1996].

If this trend is maintained throughout the stability domain of ice VII, the larger thermal conductivity of pure ice VII at higher pressures would lead to much higher values of the conductive heat flux and convective power than those calculated in Figure 5. Our main conclusion that the presence of CH_3OH substantially decreases the heat transfer in the ice shell would not be altered, but this decrease would be strongly enhanced.

The depth dependence of k may further influence the dynamics of the ice shell, an effect that was not accounted for in our calculations. Numerical models of convection applied to the Earth's mantle have indicated that an increase in thermal conductivity with depth favors the formation of large plumes and enhances heat transfer [e.g., *Matyska et al.*, 1994; *van den Berg et al.*, 2005]. Based on these numerical experiments, the increase of k with depth that we observed in our experiments may increase heat transfer through the ice mantle of super-Earths and enhance the cooling of these planets. Quantitative estimates of this effect, however, require the calculation of models of stagnant lid convection that includes depth-dependent thermal conductivity.

5. Conclusions

To summarize, we have employed the time domain thermoreflectance and stimulated Brillouin scattering coupled with diamond anvil cell techniques to investigate the thermal conductivity and sound velocity of H_2O-CH_3OH mixtures at high pressures up to 12 GPa. We find that the presence of small amounts of CH_3OH substantially reduces the thermal conductivity and sound velocity of ice VII-CH_3OH mixtures, compared to those of pure water. For fractions of CH_3OH in the range of 5–20 wt %, the thermal conductivity is reduced by about a factor of 2 to 5, depending on the fraction of CH_3OH, and the sound velocity is decreased by about a factor of 1.4. These findings may have important consequences for the heat transfer through the ice mantles of icy super-Earths. A lower thermal conductivity reduces conductive heat transfer but enhances the efficiency of heat transfer by convection compared to conduction. Overall, the presence of 10 wt % CH_3OH reduces by a factor of 2 the power that the ice mantle can transfer toward the surface, which may significantly influence the thermal history and evolution of the radial structure of the planet.

The results we presented here focus on the effects of CH_3OH on convective heat transfer through the ice mantles of super-Earths. However, the reduction in thermal conductivity at high pressures, and the reduction in the power transported by convection it induces, could be a phenomenon common to other H_2O-volatile mixtures, with possible applications to icy moons, dwarf planets, and super-Earths. Note that previous studies have shown that methanol monohydrate would exist in H_2O-CH_3OH mixtures at ambient pressure and low temperature [*Fortes and Choukroun*, 2010]. The phase stability and presence of methanol monohydrate in H_2O-CH_3OH mixtures under our current experimental conditions of room temperature and up to 12 GPa are not known; however, the presence of methanol monohydrate may become critical in the mixture at similar pressure but lower temperature environments. Recent experiments further indicate that at ambient pressure and near 273 K, the presence of methanol enhances the formation of methane clathrates, in which case methanol is incorporated in the clathrate hydrate cages [*Shin et al.*, 2013].

Future experimental measurements on the thermal conductivity, phase diagram, and other transport properties of H_2O mixed with other compounds, including ammonia and methane, under extreme pressures and a wide range of temperatures (typically, 200 to 1000 K) are needed to complete the data set of ice properties. Improvements in the modeling of heat transfer through icy shells are also required, including detailed investigations of the influence of sensitive, but uncertain parameters, such as the viscosity. Combined together,

our new experimental results and refined numerical modeling provide deeper insights into the thermal histories and evolution of the radial structures of icy super-Earths and icy bodies of the Solar System.

References

Cahill, D. G. (2004), Analysis of heat flow in layered structures for time-domain thermoreflectance, *Rev. Sci. Instrum.*, *75*, 5119–5122, doi:10.1063/1.1819431.

Cahill, D. G., W. K. Ford, K. E. Goodson, G. D. Mahan, A. Majumdar, H. J. Maris, R. Merlin, and S. R. Phillpot (2003), Nanoscale thermal transport, *J. Appl. Phys.*, *93*, 793, doi:10.1063/1.1524305.

Chen, B., W.-P. Hsieh, D. G. Cahill, D. R. Trinkle, and J. Li (2011), Thermal conductivity of compressed H_2O to 22 GPa: A test of the Leibfried-Schlömann equation, *Phys. Rev. B*, *83*, 132301, doi:10.1103/PhysRevB.83.132301.

Chizhov, V. (1993), Thermodynamic properties and thermal equations of the state of high-pressure ice phases, *J. Appl. Mech. Tech. Phys.*, *34*(2), 253–262, doi:10.1007/BF00852521.

Davaille, A., and C. Jaupart (1993), Transient high-Rayleigh-number thermal convection with large viscosity variations, *J. Fluid Mech.*, *253*, 141–166.

Deschamps, F., and J.-R. Lin (2014), Stagnant lid convection in 3D-Cartesian geometry: Scaling laws and applications to icy moons and dwarf planets, *Phys. Earth Planet. Inter.*, *229*, 40–54, doi:10.1016/j.pepi.2014.01.002.

Deschamps, F., O. Mousis, C. Sanchez-Valle, and J. I. Lunine (2010), The role of methanol on the crystallization of Titan's primordial ocean, *Astrophys. J.*, *724*, 887–894.

Durham, W. B., and L. A. Stern (2001), Rheological properties of water ice - Application to satellites of outer planets, *Annu. Rev. Earth Planet. Sci.*, *29*, 295–330.

Durham, W. B., L. A. Stern, and S. H. Kirby (1996), Rheology of water ices V and VI, *J. Geophys. Res.*, *101*, 2989–3001, doi:10.1029/95JB03542.

Eggert, J., L. Xu, R. Che, L. Chen, and J. Wang (1992), High pressure refractive index measurements of 4:1 methanol:ethanol, *J. Appl. Phys.*, *72*, 2453–2461.

Fei, Y., H.-K. Mao, and R. J. Hemley (1993), The thermal expansivity, bulk modulus, and melting curve of H_2O-ice VII to 20 GPa, *J. Chem. Phys.*, *99*, 5369–5373.

Fortes, A. D., and M. Choukroun (2010), Phase behaviour of ices and hydrates, *Space Sci. Rev.*, doi:10.1007/s11214-010-9633-3.

Ge, Z., D. Cahill, and P. Braun (2006), Thermal conductance of hydrophilic and hydrophobic interfaces, *Phys. Rev. Lett.*, *96*, 186101, doi:10.1103/PhysRevLett.96.186101.

Goncharov, A., V. Struzhkin, M. Somayazulu, R. Hemley, and H. Mao (1996), Compression of ice to 210 gigapascals: Infrared evidence for a symmetric hydrogen-bonded phase, *Science*, *273*, 218–220.

Grasset, O., C. Sotin, and F. Deschamps (2000), On the internal structure and dynamics of Titan, *Planet. Space Sci.*, *48*, 617–636.

Hodyss, R., C. Parkinson, P. Johnson, J. Stern, J. Goguen, Y. Yung, and Y. Kanik (2009), Methanol on Enceladus, *Geophys. Res. Lett.*, *36*, L17103, doi:10.1029/2009GL039336.

Hsieh, W.-P. (2015), Thermal conductivity of methanol-ethanol mixture and silicone oil at high pressures. *J. Appl. Phys.*, *117*, 235901, doi:10.1063/1.4922632.

Hsieh, W.-P., and Y. H. Chien (2015), High pressure Raman spectroscopy of H_2O-CH3OH mixtures, *Sci. Rep.*, *5*, 8532, doi:10.1038/srep08532.

Hsieh, W.-P., B. Chen, J. Li, P. Keblinski, and D. G. Cahill (2009), Pressure tuning of the thermal conductivity of the layered muscovite crystal, *Phys. Rev. B*, *80*, 180302, doi:10.1103/PhysRevB.80.180302.

Hussmann, H., C. Sotin, and J. Lunine (2007), Interiors and evolution of icy satellites, in *Treatise on Geophysics*, pp. 509–539, Elsevier, Amsterdam, doi:10.1016/B978-044452748-6.00168-1.

Kuchner, M. J. (2003), Volatile-rich Earth-mass planets in the habitable zone, *Astrophys. J.*, *596*, L105–L108.

Léger, A., et al. (2004), A new familly of planets? Ocean planets, *Icarus*, *169*, 499–504.

Mao, H. K., P. M. Bell, J. W. Shaner, and D. J. Steinberg (1978), Specific volume measurements of Cu, Mo, Pd, and Ag and calibration of the ruby R1 fluorescence pressure gauge from 0.06 to 1 Mbar, *J. Appl. Phys.*, *49*, 3276–3283, doi:10.1063/1.325277.

Matyska, C., J. Moser, and D. A. Yuen (1994), The potential influence of radiative heat transfer on the formation of megaplumes in the lower mantle, *Earth Planet. Sci. Lett.*, *125*, 255–266.

Mousis, O., L. I. Lunine, J. H. Waite, B. Magee, W. S. Lewis, K. E. Mandt, D. Marquer, and D. Cordier (2009), Formation conditions of Enceladus and origin of its methane reservoir, *Astrophys. J. Lett.*, *701*, L39–L42, doi:10.1088/0004-637X/701/1/L39.

Mumma, M. J., and S. B. Charnley (2011), The chemical composition of comets: Emerging taxonomies and natal heritage, *Annu. Rev. Astron. Astrophys.*, *49*, 471–524, doi:10.1146/annurev-astro-081309-130811.

O'Hara, K. E., X. Hu, and D. G. Cahill (2001), Characterization of nanostructured metal films by picosecond acoustics and interferometry, *J. Appl. Phys.*, *90*, 4852, doi:10.1063/1.1406543.

Pan, D., Q. Wan, and G. Galli (2014), The refractive index and electronic gap of water and ice increase with increasing pressure, *Nat. Commun.*, *5*, 3919, doi:10.1038/ncomms4919.

Pistorius, C. W. F. T., M. C. Pistorius, J. P. Blakey, and L. J. Admiraal (1963), Melting curve of ice VII up to 200 kbar, *J. Chem. Phys.*, *38*, 600–602.

Polian, A., and M. Grimsditch (1983), Brillouin scattering from H_2O: Liquid, ice VI, and ice VII, *Phys. Rev. B*, *27*, 6409.

Reese, C. C., V. S. Solomatov, J. R. Baumgardner, and W. S. Yang (1999), Stagnant lid convection in a spherical shell, *Phys. Earth Planet. Inter.*, *116*, 1–7.

Shimizu, H., T. Nabetani, T. Nishiba, and S. Sasaki (1996), High-pressure elastic properties of the VI and VII phase of ice in dense H_2O and D2O, *Phys. Rev. B*, *53*, 6107–6110, doi:10.1103/PhysRevB.53.6107.

Shin, K., K. A. Udachin, I. L. Moudrakovski, D. M. Leek, S. Alavi, C. I. Ratcliffe, and J. A. Ripmeester (2013), Methanol incorporation in clathrate hydrates and the implications for oil and gas pipeline flow assurance and icy planetary bodies, *Proc. Natl. Acad. Sci. U.S.A.*, *110*, 8437–8442.

Solomatov, V. S. (1995), Scaling of temperature-dependent and stress-dependent viscosity convection, *Phys. Fluids*, *7*, 266–274.

Sotin, C., O. Grasset, and A. Mocquet (2007), Mass-radius curve for extrasolar Earth-like planets and ocean planets, *Icarus*, *191*, 337–351.

Thomsen, C., H. T. Grahn, H. J. Maris, and J. Tauc (1986), Picosecond interferometric technique for study of phonons in the Brillouin frequency range, *Opt. Commun.*, *60*, 55–58, doi:10.1016/0030-4018(86)90116-1.

Valencia, D., D. D. Sasselov, and R. J. O'Connell (2007a), Radius and structure models of the first super-Earth planet, *Astrophys. J.*, *656*, 545–551.

Valencia, D., D. D. Sasselov, and R. J. O'Connell (2007b), Detailed models of super-Earths: How well can we infer bulk properties ?, *Astrophys. J.*, *665*, 1413–1420.

van den Berg, A. P., E. G. Rainey, and D. Yuen (2005), The combined influences of variable thermal conductivity, temperature- and pressure-dependent viscosity and core-mantle coupling on thermal evolution, *Phys. Earth Planet. Inter.*, *149*, 259–278.

Waite, J. H., Jr., et al. (2009), Liquid water on Enceladus from observations of ammonia and [40]Ar in the plume, *Nature*, *460*, 487–490, doi:10.1038/nature08153.

Yao, C., F. Deschamps, J. P. Lowman, C. Sanchez-Valle, and P. J. Tackley (2014), Stagnant lid convection in bottom-heated thin 3-D spherical shells: Influence of curvature and implications for dwarf planets and icy moons, *J. Geophys. Res. Planets*, *119*, 1895–1913, doi:10.1002/2014JE004653.

Erratum

In the originally published version of this article, equation 5 was missing the exponent 0.27. The error has since been corrected and this version may be considered the authoritative version of record.